Very high and very low Fisher information for small displacements of a plasmonic silver nanowire

de Graaff, J.B.P.; Urbach, Paul; El Gawhary, O.

DOI
10.1103/m4cm-545j

Publication date
2025

Document Version
Final published version

Published in
Physical Review Letters

Very high and very low Fisher information for small displacements of a plasmonic silver nanowire

J. B. P. de Graaff,[1,*] H. P. Urbach,[1] and O. El Gawhary[1,2]

[1]*Optics Research Cluster, Imaging Physics Department, Delft University of Technology, Van der Waalsweg 8, 2628 CH Delft, The Netherlands*
[2]*ASML Research Netherlands B.V., De Run 6501, 5504 DR Veldhoven, The Netherlands*

(Received 24 June 2025; accepted 22 October 2025; published 1 December 2025)

In this paper, we study the effects of plasmonic resonances on the Fisher information in the far field, of the position of a silver nanowire with respect to the center of a focused spot. We study theoretically a nanowire embedded in a high refractive index substrate that is illuminated by a dark-field focused spot. The position of the nanowire is determined from the scattered far-field intensities. The Fisher information is computed for both a lateral and longitudinal displacement of the nanowire, and its dependence on the illumination frequency is analyzed. The resonance frequencies of the nanowires are determined. We find that frequencies near a plasmonic resonance can enhance the Fisher information. However, at the resonance frequency itself and very close to it, the scattered far field corresponds to an *information dark state*. The phenomenon is demonstrated for silver, and the underlying physical mechanism is explained with an analytical model. As is shown, the dark state can be converted into a state with very high Fisher information about the positions of the nanowire by modifying the focused spot.

DOI: 10.1103/m4cm-545j

I. INTRODUCTION

Optical metrology plays a key role in many modern applications such as biomedical imaging or semiconductor manufacturing. In the field of optical metrology, an incidence beam illuminates an unknown target, and the intensity of the scattered light is measured at a detector usually positioned in the far field. The aim is to estimate the properties of the unknown target from the far-field measurements. In the field of semiconductor manufacturing, the unknown target is typically a periodic grating of which some feature must be determined [1,2].

The measurements in the far field are always subject to Poisson shot noise; hence, there is a fundamental limit to the precision of the estimates. This limit is quantified by the Cramér-Rao lower bound (CRLB), which gives us a lower bound on the precision of a minimum-variance unbiased estimator based on the measured intensities. A lower CRLB means a more precise estimator. The CRLB is given by the reciprocal of the square root of the Fisher information, so a high Fisher information means a low CRLB.

The CRLB has been studied in various optical applications, including the localization of single particles [3,4], ptychography [5,6], the design of metagratings [7], coherent diffractive imaging [8], and wave front shaping [9]. Other recent works on Fisher information and the CRLB in optics include Ref. [10], where it is shown that the scattering environment of a particle does not influence the Fisher information of its properties, and Ref. [11], where a continuity equation for the Fisher information is introduced.

The influence of the target's intrinsic optical properties (specifically, the presence of plasmonic resonances) on the CRLB has however not yet been explored.

In this work, we investigate how plasmonic resonances in a silver nanowire influence the Fisher information and hence the CRLB. We consider an infinite nanowire embedded in a high refractive index substrate, illuminated by a cylindrical lens that generates a one-dimensional focused spot. A high refractive index, comparable to that of silicon, is needed for the ambient medium to guarantee that the nanowire has a plasmonic resonance. The scattered intensities are determined within a certain numerical aperture of a detector in the far field, and the Fisher information is computed with respect to the lateral and longitudinal displacement of the nanowire. The (complex) resonance frequencies of the nanowire are computed under the assumption of the Drude model for the permittivity of silver.

Our results show that when the illumination frequency is close to a plasmonic resonance, the Fisher information is larger than for nonresonant frequencies, leading to a more precise estimator. (Fisher information with respect to a lateral shift is between $\sim 10^{18}$ and $\sim 10^{19}\,\mathrm{m}^2$ for a nonresonant nanowire made of Cr, compared to between $\sim 10^{20}$ and $\sim 10^{22}\,\mathrm{m}^2$ for the resonant nanowire of Ag, both for a laser with power 2 mW.) However, at the resonance frequency itself and extremely close to it, an *information dark state* emerges, where no information on either the transverse or the longitudinal position is present in the far-field measurements. It is found that by changing the illumination, the information dark state can be eliminated. This is shown through a simplified analytical model similar to analyses done in Refs. [12,13].

*Contact author: J.B.P.deGraaff@tudelft.nl

This paper is structured as follows. In Sec. II, the Fisher information and Cramér-Rao lower bound are defined and computed for the case of an illumination and detection system. In Sec. III, the dark-field illumination system that we use is defined. In Sec. IV, the model of our scattering is explained. In Sec. V, the theory of plasmonic resonances for the nanowire is explained. In Sec. VI, the occurence of the information dark state is demonstrated for the silver nanowire. The cause of the dark state is explained in Sec. VII. In Sec. VIII, the illumination is changed with a phase shift, and it shown that the dark state is changed into a state with high Fisher information. In Sec. IX, it is discussed how the material of the substrate and the radius of the wire affect the results. It is also explained how the results can be used for extremely precise position around the optical axis. Finally, the conclusions are in Sec. X.

II. FISHER INFORMATION AND CRAMÉR-RAO LOWER BOUND FOR POISSON SHOT NOISE

Typically, in statistics, a number of samples $\{x_1, \ldots, x_M\}$ are drawn from a probability distribution with probability density function (pdf) $f(x|\theta)$. The pdf depends on an unknown parameter θ, which is to be estimated from the samples. In our case, these samples are the intensities measured by the pixels of the detector in the far field, and the parameter θ is a transverse or longitudinal displacement of the nanowire. The *estimator* for θ is a function of the samples and is denoted by $\hat{\theta}$,

$$\hat{\theta} = \hat{\theta}(x_1, \ldots, x_M). \tag{2.1}$$

Let $\mathbb{E}$ denote the expected value. The estimator is called *unbiased* if

$$\mathbb{E}[\hat{\theta}] = \theta,$$

where θ is the true value of the parameter, and it is called *biased* if

$$\mathbb{E}[\hat{\theta}] \neq \theta.$$

For many applications, it is crucial to understand how precise the estimator is for the parameter θ. In fact, we look for the *minimum variance unbiased estimator*. This is an estimator $\hat{\theta}$ such that $\hat{\theta}$ is unbiased and

$$\mathbb{E}[|\hat{\theta} - \mathbb{E}[\hat{\theta}]|^2] \tag{2.2}$$

is minimal. A lower bound on the variance of the estimator [Eq. (2.2)] is given by the reciprocal of the *Fisher information*. Given the pdf, the *Fisher information* of the probability distribution can be computed. Denote by $\mathbb{E}_\theta$ the expectation conditional on θ. This means that the parameter θ, upon which the model depends, is assumed to be deterministic in this expectation. The Fisher information $\mathcal{J}_\theta$ is then given by

$$\mathcal{J}_\theta = \mathbb{E}_\theta\left[\left(\frac{d}{d\theta}\log f(x|\theta)\right)^2\right]. \tag{2.3}$$

It is important to note here that the Fisher information $\mathcal{J}_\theta$ still depends on the true value of the parameter θ, and therefore it is a function of θ. In this notation, we have

$$\sqrt{\mathbb{E}[|\hat{\theta} - \mathbb{E}[\hat{\theta}]|^2]} \geqslant \mathcal{J}_\theta^{-1/2}. \tag{2.4}$$

This is called the CRLB. So the higher the Fisher information, the lower the CRLB, and hence the more precise an estimator can be.

We assume that our measurements are limited by the Poisson shot noise. Then the probability mass function for the number of photons is given by the Poisson distribution. Let ω be the frequency of the light. If the detector consists of K pixels and the power measured by pixel k is P_k, the number of photons per unit of time measured by this pixel is

$$N_k = \frac{P_k}{\hbar\omega}. \tag{2.5}$$

For each k, the expected value of N_k is denoted by n_k, and it depends on the parameter θ of the target,

$$\mathbb{E}[N_k] = n_k = n_k(\theta). \tag{2.6}$$

The probability that the detected number of photons N_k is equal to m is

$$\mathbb{P}(N_k = m) = \frac{n_k^m}{m!}e^{-n_k}. \tag{2.7}$$

Using Eqs. (2.3) and (2.7), we can compute the Fisher information with respect to θ first at a single pixel k

$$\mathcal{J}_\theta(k) = \frac{1}{n_k(\theta)}\left(\frac{d}{d\theta}n_k(\theta)\right)^2 = \frac{1}{\hbar\omega}\frac{1}{P_k(\theta)}\left(\frac{d}{d\theta}P_k(\theta)\right)^2. \tag{2.8}$$

The Poisson shot noise is independent for all the pixels. Hence, the total Fisher information of all the pixels is obtained by summing Eq. (2.8) over all the pixels:

$$\mathcal{J}_\theta = \sum_{k=1}^{K}\mathcal{J}_\theta(k). \tag{2.9}$$

III. MODEL OF THE DARK-FIELD SETUP

We consider the scattering by a long metallic nanowire embedded in a substrate of high refractive index. We use the coordinate system (x, y, z) shown in Fig. 1, with the z axis equal to the optical axis, z being positive in the direction of the incident field and with the y axis equal to the axis of the nanowire.

The nanowire is placed inside of the substrate, at a focal distance f from the lens (this includes the height of the substrate; see Fig. 1). It is illuminated by a cylindrical spot obtained by focusing a TM (transverse magnetic) polarized plane wave by a cylindrical lens. TM polarization means that the magnetic field is parallel to the y axis (the axis of the cylinder). The polarization and a high index medium surrounding the cylinder are chosen such that a plasmonic resonance exists. When the nanowire is considered to be infinitely long, the total field is also TM polarized, and we shall therefore use the magnetic field component H_y everywhere below.

The wavelength of the illumination is varied between 550 and 900 nm. We shall consider subsequently the models for the illumination, the scattering by the wire, and the detection. The time dependence of all fields is given by $e^{-i\omega t}$, and $k = \frac{\omega}{c}$ will be the wave number in vacuum.

The refractive index of the surrounding medium is taken to be $n = 4.0$ for all of the wavelengths and the radius of

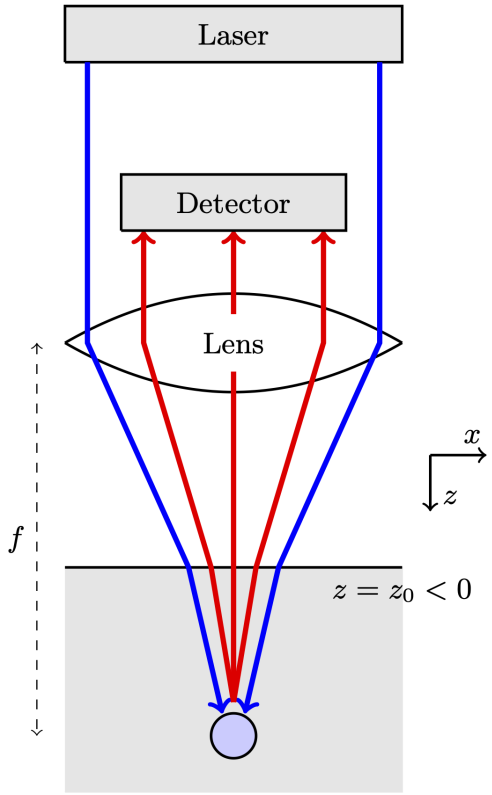

FIG. 1. Considered configuration with dark-field illumination using a cylindrical lens of a metallic nanowire embedded in a high refractive index substrate. The cylindrical spot is TM polarized; i.e., the magnetic field is parallel to the y direction in order to excite a plasmon in the metallic wire.

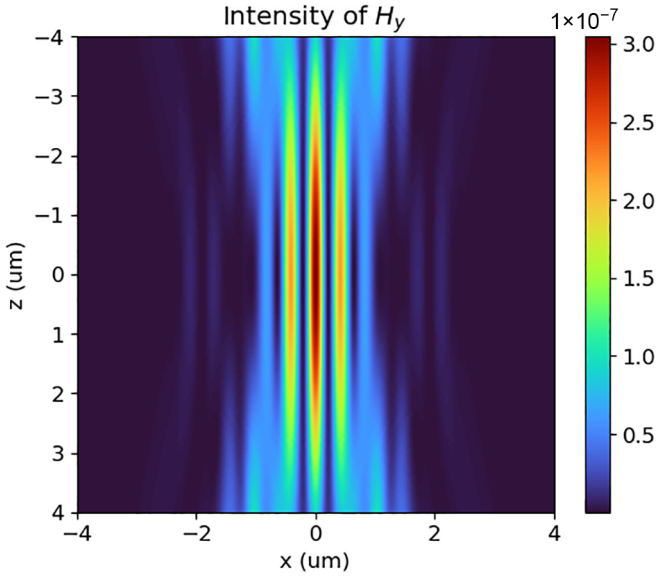

FIG. 2. The modulus squared of H_y inside the silicon substrate, at a grid ranging from -4 to $+4$ μm in both directions around the focus point, which is at the origin. The illumination angles in degrees are $\theta_{\min} = 30^\circ$ and $\theta_{\max} = 50^\circ$. The transmission through the air-silicon interface has been taken into account. In this plot, no nanowire is present.

the wire is $a = 20\,\text{nm}$. The refractive index of the substrate is comparable to that of silicon at a wavelength of around 600 nm. The radius is chosen such that it is subwavelength, but not so small that it scatters like a point dipole [12]. The material of the nanowire is silver under the Drude model. Incident light transmits through the surface of the substrate, then focuses at the center of the nanowire, where it is scattered by it.

A plot of the modulus squared of the H_y field at the focus point for this dark-field illumination is given in Fig. 2. Due to not having the full lens for the illumination, we see large lobes around the focus. The spot is also more elongated in the z direction.

IV. MODEL OF THE SCATTERING

We consider a coordinate system (x, y, z) with the z axis along the optical axis and pointing in the direction of the incident light. The nanowire is inside the substrate and its center is at the origin of the coordinate system. The interface is at $z = z_0$, with $z_0 < 0$. The incident spot is expanded into TM-polarized plane waves, and the transmission through the interface is taken into account of using the Fresnel coefficient. The plane waves that are incident on the nanowire are expanded into Bessel radial modes. The Hankel modes that are generated by the scattering of Bessel modes by the cylinder are expanded in plane waves to take account of the transmission by the interface.

A. Dark-field illumination

In this subsection, the dark-field illumination is explained, as well as the transmission of the illumination through the air-silicon interface.

In our dark-field illumination setup, the outer part of the lens is chosen for the illumination of the nanowire, and the inner part for the detection (see Fig. 3). This is done so that the reflection from the incident beam off the substrate and onto the detector does not interfere with the scattered field that results from the nanowire. The permittivity of free space is denoted by $\varepsilon = 1$ and the (real) permittivity of the substrate is denoted by ε_1.

The cylindrical lens is parametrized by x components k_x^i of the incident wave vectors $\mathbf{k}^i$. Because we only illuminate with the outer part of the lens, it has an inner numerical aperture NA_{inner} and an outer numerical aperture NA_{outer}, with $0 < \text{NA}_{\text{inner}} < \text{NA}_{\text{outer}} < 1$. We denote

$$K = \{k_x^i : \text{NA}_{\text{inner}} < |k_x^i/k| < \text{NA}_{\text{outer}}\} \tag{4.1}$$

and

$$k_z^i = \sqrt{k^2\varepsilon - \left(k_x^i\right)^2}. \tag{4.2}$$

We write P for the total power of the incident light, in units of watts (W), d_x for the length of one side of the lens in the x direction in units of meters (m), and d_y for the length of the lens in the y direction in units of meters (m). The amplitude of

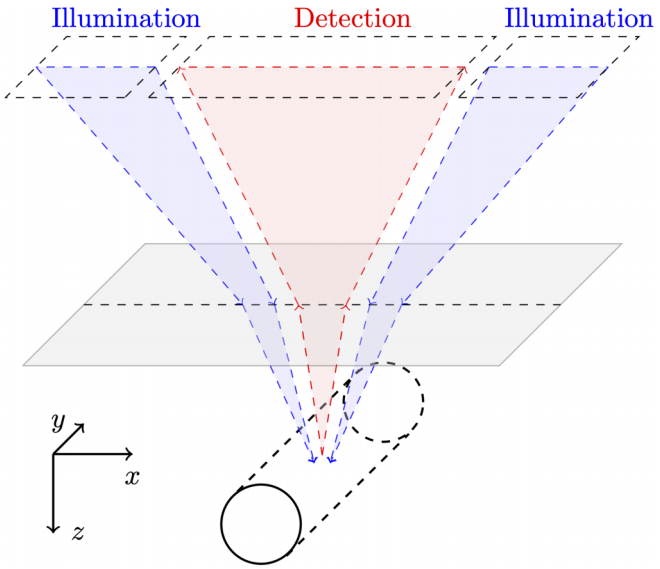

FIG. 3. A sketch of the illumination and detection setup. The nanowire inside the substrate is illuminated with a focused spot from the outer parts of the lens in the far field. The scattered field is detected in the center part of the pupil.

the incident field is given by

$$A^{\text{in}} = \left(2\sqrt{\frac{\varepsilon_0}{\mu_0}}\frac{P}{2d_x d_y}\right)^{1/2} (\text{A m}^{-1}). \tag{4.3}$$

The incident field after the lens is

$$H_y^{\text{in}}(x,z) = -\frac{ife^{-ikf}}{2\pi}A^{\text{in}}\int_K \frac{1}{k_z^i}e^{i\mathbf{k}^i\cdot\mathbf{r}}\,dk_x^i, \tag{4.4}$$

with $\mathbf{k}^i = (k_x^i, k_z^i)^T$. The plane waves in the integral [Eq. (4.4)] propagate in the positive z direction toward the interface at $z = z_0 < 0$. At the interface, each plane wave picks up a transmission coefficient $t^p(k_x^i)$ and a phase shift. The phase shift is because the interface is not located at $z = 0$, for which typically the Fresnel coefficients are computed. The wave vector inside the substrate (after transmission) is given by $\mathbf{k}_1^i = (k_x^i, k_{1z}^i)^T$, with

$$k_{1z}^i = \sqrt{k^2\varepsilon_1^2 - \left(k_x^i\right)^2}. \tag{4.5}$$

The transmission and reflection coefficients in TM polarization (or p polarization) are given by

$$r^p(k_x) = \frac{\varepsilon_1 k_z - \varepsilon k_{1z}}{\varepsilon_1 k_z + \varepsilon k_{1z}}, \quad t^p(k_x) = \frac{2\varepsilon_1 k_z}{\varepsilon_1 k_z + \varepsilon k_{1z}}. \tag{4.6}$$

The part of the incident field that transmits through the air-silicon interface is given by

$$H_y^t(x,z) = -\frac{ife^{-ikf}}{2\pi}A^{\text{in}}\int_K \frac{t^p(k_x^i)}{k_{1z}^i}e^{i(k_z^i - k_{1z}^i)z_0}e^{i\mathbf{k}_1^i\cdot\mathbf{r}}\,dk_x^i, \tag{4.7}$$

The part of the incident field that reflects off the substrate and propagates back to the lens is given by

$$H_y^r(x,z) = -\frac{ife^{-ikf}}{2\pi}A^{\text{in}}\int_K \frac{r^p(k_x^i)}{k_z^i}e^{2ik_z^i z_0}e^{i\mathbf{k}^i\cdot(x,-z)^T}\,dk_x^i. \tag{4.8}$$

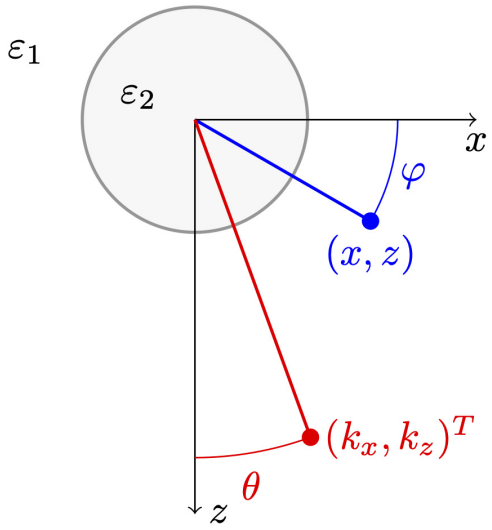

FIG. 4. A sketch of the polar coordinate systemused in the analytical computation of the field scattered by the nanowire. The incident light propagates in the positive z direction, the fields and the nanowire are independent of y.

This is a superposition of plane waves propagating in the negative z direction, with k_x between $\pm k\text{NA}_{\text{inner}}$ and $\pm k\text{NA}_{\text{outer}}$. However, the far-field detection is chosen in such a way that only angles with $\mathbf{k}$ within NA_{det} are detected, with $\text{NA}_{\text{det}} < \text{NA}_{\text{inner}}$. So, the reflected field [Eq. (4.8)] is not detected.

B. Scattering of the incidence field by the nanowire

In this subsection, the scattering of the incident field [Eq. (4.7)] by the nanowire is determined. A cylindrical coordinate system (r, φ, y) is introduced such that $x = r\cos\varphi$ and $z = r\sin\varphi$ (see Fig. 4). The nanowire is independent of y and has radius $r = a$. The permittivity of the metal is ε_2. The refractive indices are $n_1 = \sqrt{\varepsilon_1}$ and $n_2 = \sqrt{\varepsilon_2}$. All of the fields that we consider are time harmonic with time dependence given by $\exp(-i\omega t)$, with frequency $\omega > 0$. Set $k = \omega/c$ for the waven umber in vacuum, with c the speed of light in vacuum. In TM polarization, the incident $\mathbf{H}$ field only has a nonzero y component. Under these assumptions, Maxwell's equations reduce to a scalar Helmholtz equation for the total H_y field, from which all other field components can be determined. We have

$$\nabla^2 H_y(r,\varphi) + k^2\varepsilon_1 H_y(r,\varphi) = 0, \quad r > a, \tag{4.9}$$

$$\nabla^2 H_y(r,\varphi) + k^2\varepsilon_2 H_y(r,\varphi) = 0, \quad r < a. \tag{4.10}$$

The following conditions hold on the boundary of the cylinder $r = a$:

$$\lim_{r\downarrow a} H_y(r,\varphi) = \lim_{r\uparrow a} H_y(r,\varphi), \tag{4.11}$$

$$\lim_{r\downarrow a}\frac{1}{\varepsilon_1}\frac{\partial H_y}{\partial r} = \lim_{r\uparrow a}\frac{1}{\varepsilon_2}\frac{\partial H_y}{\partial r}. \tag{4.12}$$

The solution to Eqs. (3.9) and (4.10) is found by expanding the field H_y into radial Hankel and Bessel modes, inside and outside of the nanowire, respectively. The coefficients of the radial modes are then computed using the matching conditions

at $r = a$. The full expression for the solution is given in Chapter 2 of Ref. [14].

A general incident field can be decomposed into Bessel modes,

$$H_y^{\text{in}}(r,\varphi) = \sum_{m=-\infty}^{+\infty} A_m^{\text{in}} J_m(kn_1 r) e^{im\varphi}. \tag{4.13}$$

The total field outside of the wire is the sum of the incident and scattered field, where the latter can be expanded in modes containing Hankel functions of the first kind because these satisfy the outgoing radiation condition:

$$H_y(r,\varphi) = [t] \sum_{m=-\infty}^{+\infty} \left[A_m^{\text{in}} J_m(kn_1 r) + A_m^{\text{in}} B_m H_m^{(1)}(kn_1 r)\right] e^{im\varphi}, \quad r > a, \tag{4.14}$$

In the above, $H_m^{(1)}$ is the Hankel function of the first kind of order m. The total field inside the wire can be written as

$$H_y(r,\varphi) = \sum_{m=-\infty}^{+\infty} A_m^{\text{in}} C_m J_m(kn_2 r) e^{im\varphi}, \quad r < a \tag{4.15}$$

The coefficients B_m and C_m are, for TM polarization, given by

$$B_m = \frac{\frac{k}{n_2} J_m(k_1 a) J_m'(k_2 a) - \frac{k}{n_1} J_m'(k_1 a) J_m(kn_2 a)}{\frac{k}{n_1} J_m(k_2 a) H_m^{(1)\prime}(k_1 a) - \frac{k}{n_2} J_m'(k_2 a) H_m^{(1)}(k_1 a)}, \tag{4.16}$$

$$C_m = \frac{\frac{k}{n_1} J_m(k_1 a) H_m^{(1)\prime}(k_1 a) - \frac{k}{n_1} J_m'(k_1 a) H_m^{(1)}(k_1 a)}{\frac{k}{n_1} J_m(k_2 a) H_m^{(1)\prime}(k_1 a) - \frac{k}{n_2} J_m'(k_2 a) H_m^{(1)}(k_1 a)}, \tag{4.17}$$

with the abbreviation $k_1 = kn_1$ and $k_2 = kn_2$. For incident field (4.7), the coefficients A_m^{in} are given by

$$A_m^{\text{in}} = \int_K \frac{a^p(k_x^i)}{k_{1z}} e^{im \arctan(k_x^i/k_{1z})}\, dk_x^i, \tag{4.18}$$

with amplitude function

$$a^p(k_x^i) = -\frac{ife^{-ikf}}{2\pi} A^{\text{in}} t^p(k_x^i) e^{i(k_z^i - k_{1z}^i)z_0}. \tag{4.19}$$

The scattered field outside of the wire and inside the substrate is given by the part of the total field containing the Hankel modes, since these satisfy outgoing radiation condition:

$$H_y^s(r,\varphi) = \sum_{m=-\infty}^{+\infty} A_m^{\text{in}} B_m H_m^{(1)}(kn_1 r) e^{im\varphi}. \tag{4.20}$$

C. Scattered field at the detector

To compute the scattered field at the detector, the field (4.20) is expanded into plane waves again. These plane waves are partially transmitted and reflected by the interface (see Fig. 5). We use the plane wave expansion of the Hankel modes for $z < 0$. We write $\mathbf{k}^s = (k_x, -k_{1z})^T$, $\theta_s = \arctan(k_x/k_{1z})$, and $\mathbf{r} = r(\cos\varphi, \sin\varphi)^T$:

$$H_m^{(1)}(kn_1 r) e^{im\varphi} = \frac{i^{-m}}{\pi} \int_{-kn_1}^{kn_1} \exp(i\mathbf{k}^s \cdot \mathbf{r} + im(\theta_s - \pi/2)) \frac{dk_x}{k_{1z}} \tag{4.21}$$

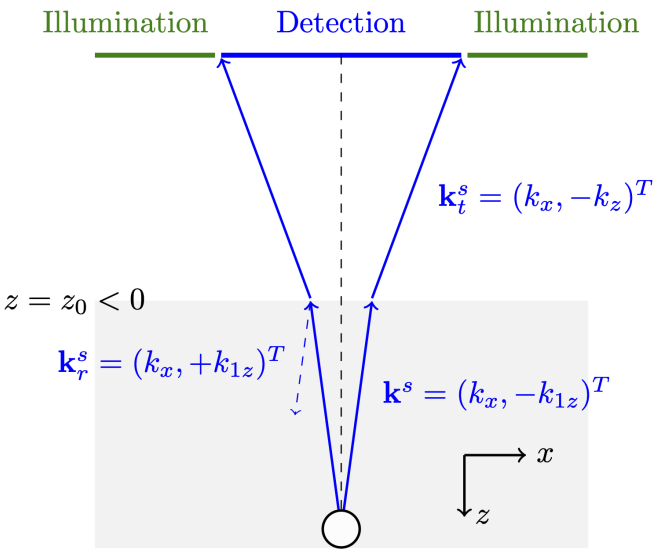

FIG. 5. The wave vectors $\mathbf{k}^s$, $\mathbf{k}_r^s$, and $\mathbf{k}_t^s$ of the scattered field, reflected scattered field, and scattered field transmitted through the interface.

$$= \frac{(-1)^{-m}}{\pi} \int_{-kn_1}^{kn_1} \exp(i\mathbf{k}^s \cdot \mathbf{r} + im\theta_s) \frac{dk_x}{k_{1z}}. \tag{4.22}$$

The scattered field, for $z < 0$, is given by

$$H_y^s(r,\varphi) = \frac{1}{\pi} \sum_{m=-\infty}^{+\infty} (-1)^m A_m^{\text{in}} B_m \int_{-kn_1}^{+kn_1} e^{i\mathbf{k}^s \cdot \mathbf{r} + im\theta_s} \frac{dk_x}{k_{1z}} \tag{4.23}$$

$$= \frac{1}{\pi} \int_{-kn_1}^{+kn_1} \left(\sum_{m=-\infty}^{+\infty} (-1)^m A_m^{\text{in}} B_m e^{im\theta_s} \right) e^{i\mathbf{k}^s \cdot \mathbf{r}} \frac{dk_x}{k_{1z}} \tag{4.24}$$

$$= \frac{1}{\pi} \int_{-kn_1}^{+kn_1} \mathcal{F}(k_x, k_{1z}) e^{i\mathbf{k}^s \cdot \mathbf{r}} \frac{dk_x}{k_{1z}}. \tag{4.25}$$

Here, we have written

$$\mathcal{F}(k_x, k_{1z}) = \sum_{m=-\infty}^{+\infty} (-1)^m A_m^{\text{in}} B_m e^{im\theta_s}, \tag{4.26}$$

with $\theta_s = \arctan(k_x/k_{1z})$. The field (4.25) propagates toward the interface, where it now transmits through the interface to the detector. Similar to before, each plane wave is now also multiplied by a phase shift and a transmission coefficient. The transmission and reflection coefficients in TM polarization, for the plane waves from the substrate into free space, are given by

$$r^p(k_x) = \frac{\varepsilon k_{1z} - \varepsilon_1 k_z}{\varepsilon_1 k_z + \varepsilon k_{1z}}, \quad t^p(k_x) = \frac{2\varepsilon k_{1z}}{\varepsilon_1 k_z + \varepsilon k_{1z}}. \tag{4.27}$$

After transmission through the interface, the scattered field (4.25) becomes in free space

$$H_y^{s,t}(x,z) = \frac{1}{\pi} \int_{-k}^{+k} \mathcal{F}(k_x, k_z)\, e^{-ik_{1z}z_0} t^p(k_x)\, e^{i\mathbf{k}_t^s \cdot \mathbf{r}_0} \frac{dk_x}{k_z}, \tag{4.28}$$

with $\mathbf{k}_t^s = (k_x, -k_z)^T$ and $\mathbf{r}_0 = (x, z - z_0)^T$. The far-field detector is parametrized by the k_x. We detect the intensities of the plane waves with

$$-k\mathrm{NA}_{\mathrm{det}} < k_x < +k\mathrm{NA}_{\mathrm{det}}. \tag{4.29}$$

The scattered far field is given by

$$H_y^{\mathrm{FF}}(k_x) = \frac{1}{\pi}\mathcal{F}(k_x, k_z)\, e^{-ik_{1z}z_0}\frac{t^p(k_x)}{k_z}. \tag{4.30}$$

Due to the lens, the field is corrected with a factor k_z/f, leading to a far field at the detector

$$H_y^{\mathrm{det}}(k_x) = \frac{1}{\pi f}t^p(k_x)\mathcal{F}(k_x, k_z)\, e^{-ik_{1z}z_0}. \tag{4.31}$$

There is also a part of the scattered field that reflects back off the interface, into the substrate. This reflected, scattered field is given by

$$H_y^{s,r}(x, z) = \frac{1}{\pi}\int_{-kn_1}^{+kn_1}\mathcal{F}(k_x, k_{1z})\, e^{-ik_{1z}z_0}r^p(k_x)e^{i\mathbf{k}_r^s\cdot\mathbf{r}_0}\,\frac{dk_x}{k_{1z}}, \tag{4.32}$$

with $\mathbf{k}_r^s = (k_x, k_{1z})^T$. This field propagates back to the wire, where it scatters again. For typical parameters $f = 10^{-2}$ m, $z_0 = 10 \times 10^{-6}$ m, and incident wavelength $\lambda = 632$ nm, the intensity of the back-reflected scattered field at the wire is two orders of magnitude smaller than the intensity of the initial focus, and hence its scattering by the nanowire can be neglected.

In order to compute the expectation for the number of photons per pixel at the detector, the power at the pixels of the detector needs to be computed. Let k_x be the x component of the k vector corresponding to a pixel ℓ in the detector. Once the scattered field $\mathbf{H}^{\mathrm{det}}(k_x)$ has been computed, the power at pixel ℓ is given by

$$P_\ell = \frac{1}{2}\sqrt{\frac{\mu_0}{\varepsilon_0}}|\mathbf{H}^{\mathrm{det}}(k_x)|^2 \cdot A_{\mathrm{pixel}}, \tag{4.33}$$

with A_{pixel} denoting the surface area of the pixel. Dividing P_ℓ by $\hbar\omega$ gives the expected number of photons at pixel ℓ.

V. PLASMONIC RESONANCES FOR THE NANOWIRE

Plasmonic resonances in an infinite metallic nanowire arise from collective oscillations of free electrons. The occurrence of a plasmonic resonance depends on the permittivity of the nanowire and the ambient medium. These resonances are solutions to the problem [Eqs. (4.9) and (4.10)] without an incidence field.

The permittivity for which a plasmonic resonance occurs is usually derived in the static limit, such that only solutions to the Laplace equation need to be found for $r < a$ and $r > a$. In the static limit, this condition on the permittivity of the nanowire is [15]

$$\varepsilon_2 = -\varepsilon_1. \tag{5.1}$$

This relation shows that for a resonance to exist, a metal with high conductivity (i.e., strongly negative real part of the permittivity) must be surrounded by a dielectric with high positive permittivity such as silicon.

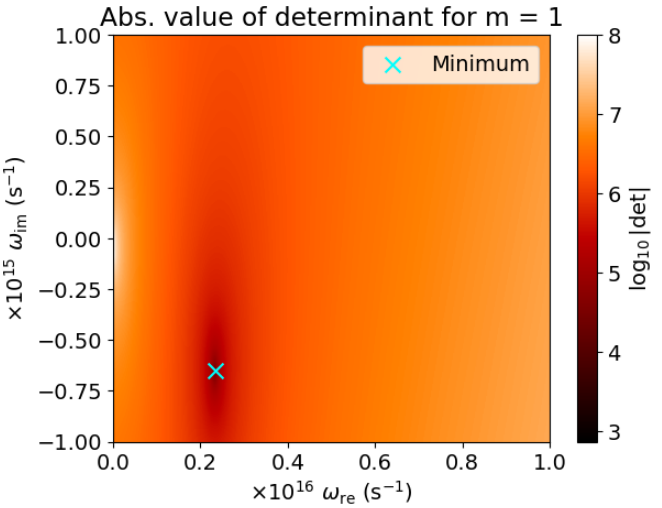

FIG. 6. Plot of the determinant for $m = 1$, as a function of the real and complex part of the frequency $\omega = \omega_{\mathrm{r}} + i\omega_{\mathrm{i}}$. The resonance frequency is marked by the cyan cross, at $\omega_{\mathrm{res}} = 2.330 \times 10^{15}$ to $6.497 \times 10^{14} i$ s^{-1}. This is for Ag under the Drude model.

The approach we use to determine the resonances does not require taking the static limit. The conditions on the nanowire to support a resonance are determined from the matching conditions on the boundary without an incident field. It is found that there is a resonance if it holds that

$$-\frac{k}{n_2}J_m'(kn_2a)H_m^{(1)}(kn_1a) + \frac{k}{n_1}H_m^{(1)\prime}(kn_1a)J_m(kn_2a) = 0, \tag{5.2}$$

for some m. The above equation is explained in detail in the Appendix. We use the Drude model for the dispersion of ε_2. For ω_p the plasma frequency of the material and γ the damping rate of the material, we set

$$\varepsilon_2(\omega) = 1 - \frac{\omega_p^2}{\omega^2 + i\gamma\omega}. \tag{5.3}$$

After substitution, the determinant in Eq. (5.2) depends on the frequency ω through k and the refractive index n_2. Hence, the frequency ω of the incidence light at which there is a resonance can be found by finding the zeros of Eq. (5.2) as a function of complex ω.

As an example, we consider a nanowire made of silver (Ag) with radius $a = 20$ nm, with $\omega_p = 1.293 \times 10^{16}$ s^{-1} and $\gamma = 7.956 \times 10^{13}$ s^{-1} in the Drude model. These values are computed by equating the real and imaginary part of $n_2(\omega)$ in the Drude model with the true refractive index, at a wavelength $\lambda = 587.6$ nm.

The absolute value of the determinant (5.2) for $m = 1$ is plotted in $\log_{10}$ scale in Fig. 6. For all m, the resonance frequencies all have a negative imaginary part. Since our time dependence was given by $\exp(-i\omega t)$, a negative imaginary part of the frequency corresponds to exponential decay.

The real part of the resonance frequency from Fig. 6 corresponds to a wavelength of $\lambda = 808.3$ nm. When only the real

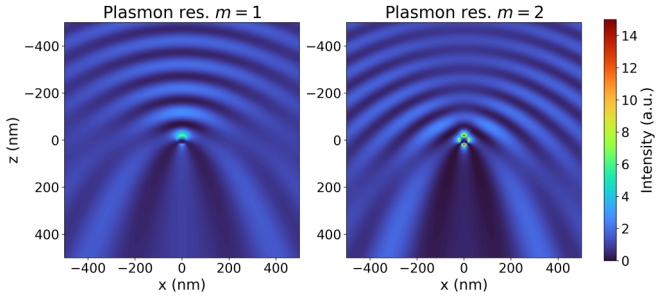

FIG. 7. The modulus squared of the total **H** field for the Ag wire with radius $a = 20$ nm, illuminated by a single plane wave with unit amplitude, propagating in the direction of the positive z axis. In the left plot, we take wavelength $\lambda = 808.3$ nm, corresponding to the real part of the resonance frequency for $m = 1$. In the right plot, the wavelength corresponding to the real part of the resonance frequency for $m = 2$ is $\lambda = 668.1$ nm.

part of the resonance frequency is substituted into the Drude model, the permittivity is $\varepsilon(\omega) = -29.7 + 1.04i\ \mathrm{s}^{-1}$.

For $m = 2$, we have $\omega_{\mathrm{res}} = 2.818 \times 10^{15}$ to $9.627 \times 10^{13} i\ \mathrm{s}^{-1}$. The real part here gives a wavelength of $\lambda = 668.1$ nm with $\varepsilon(\omega) = -20.0 + 0.59i$. For both frequencies, we plot the scattered near field in Fig. 7.

We can see from Fig. 7 that the resonance for $m = 1$ gives dipole scattering and $m = 2$ gives quadrupole scattering.

It is noted that as m gets large, the frequencies accumulate around $\omega = 3.133 \times 10^{15}$ to $3.976 \times 10^{13} i\ \mathrm{s}^{-1}$. The permittivity that the Drude model gives at this frequency is $\varepsilon(\omega) = -16.072 + 0.43420i$. This is very close to the resonance permittivity derived in the static limit (5.1).

VI. RESULTS FOR A SILVER NANOWIRE

We consider a silver (Ag) nanowire with radius $a = 20$ nm embedded in the substrate. The permittivity of Ag under the Drude model is plotted in Fig. 8. For both frequencies we plot the scattered near-field in Fig. 7. Animations of the fields are in the supplemental material [16]. We set the distance of the center of the cylinder to the surface of the substrate at 10 μm. The distance of the cylindrical illumination lens to the interface is set at 10^{-2} m. The cylindrical lens has dimensions $d_x = 2.4 \times 10^{-2}$ m in the x direction and $d_y = 2.4 \times 10^{-3}$ m in the y direction, and we are illuminating only with the outer parts of the lens (in the x direction, so from 0.6×10^{-2} m to 1.2×10^{-2} m, and from -1.2×10^{-2} m to -0.6×10^{-2} m). This means that the NA has minimum of 0.36 and maximum of 0.77. The power of light focused by the lens is 2.0 mW.

The detector is placed in the far field and detects only angles within NA 0.3; hence, it does not detect the field that is directly reflected at the surface of the substrate, and all the field detected originates from the nanowire. We assume that the detector has 2000×200 pixels, with a spacing between the pixels of 20% of both the length in the x direction and the y direction. This gives each pixel a surface area of $10\ \mu\mathrm{m} \times 10\ \mu\mathrm{m}$.

The Fisher information with respect to both the shift in the x direction and the z direction is computed numerically with a central finite difference.

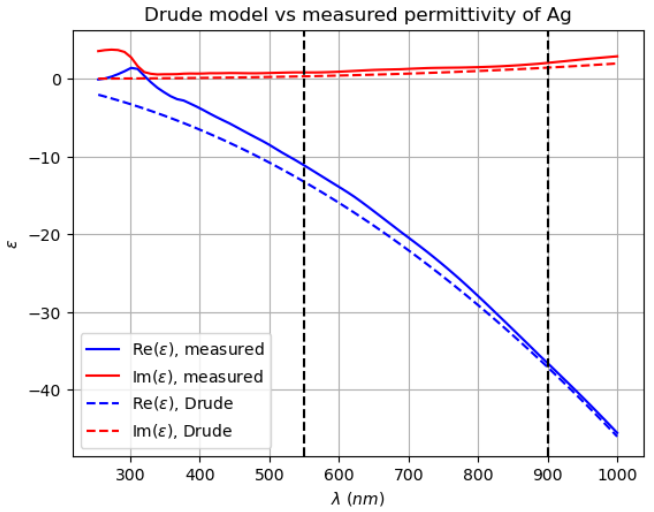

FIG. 8. The real and imaginary parts of the permittivity of silver as a function of the wavelength under the Drude model, compared with the measured permittivity. We are interested in wavelengths between 550 and 900 nm, marked by the dashed vertical lines.

In the following plots, the frequency of the incident field ω is varied between 2.093×10^{15} and $3.425 \times 10^{15}\ \mathrm{s}^{-1}$. This corresponds to wavelengths between 900 and 550 nm. The Fisher information is plotted for the x shift and the z shift, both in $\log_{10}$ base, in the left of Fig. 9. The expected total number of photons detected is plotted in the right of Fig. 9. The corresponding CRLB is shown in Fig. 10.

In Fig. 9, the real parts of the complex resonance frequencies $\omega_{\mathrm{res}}^{(m)}$ for $m = 1, 2$ are marked by the dashed lines. We note that the effect of the dipole resonance ($m = 1$) does not have a significant effect on the Fisher information. This is because the imaginary part of $\omega_{\mathrm{res}}^{(1)}$ is $\sim 6.5 \times 10^{14}\ \mathrm{s}^{-1}$, while the imaginary part of $\omega_{\mathrm{res}}^{(2)}$ is $\sim 9.6 \times 10^{13}\ \mathrm{s}^{-1}$, and hence closer to the real axis.

It can be seen in the plot that the Fisher information reaches its maximum near the real part of the quadrupole resonance frequency, but has a sharp local minimum at the real part of the resonance frequency. This is because the asymmetry of the scattered field, caused by a shift in the (positive or negative) direction, flips right at the resonance frequency. We visualize this by comparing the intensities at each pixel of the detector, for both a $+\Delta x$ shift and a $-\Delta x$ shift. To do this, we plot the following quantities as a function of ω and the scattering direction k_x:

$$I^{-\Delta x}(\omega, k_x) - I(\omega, k_x), \quad I^{+\Delta x}(\omega, k_x) - I(\omega, k_x). \tag{6.1}$$

Here, we define $I(\omega, k_x)$ as the intensity of the scattered light [the absolute value squared of Eq. (4.31)] for a frequency ω and scattering direction k_x, when the center of the wire is on the optical axis. $I^{\pm\Delta x}$ is the intensity of the scattered light for a nanowire shifted in the x direction with shift $\pm\Delta x$. The results, two 2D plots of the scattered intensity differences, are shown in Fig. 11.

From Fig. 11, it can be clearly seen that the asymmetry caused by a shift in the x direction is maximal for ω close to the real part of $\omega_{\mathrm{res}}^{(2)}$, but exactly at and very close to the real part of the resonance frequency itself, there is only

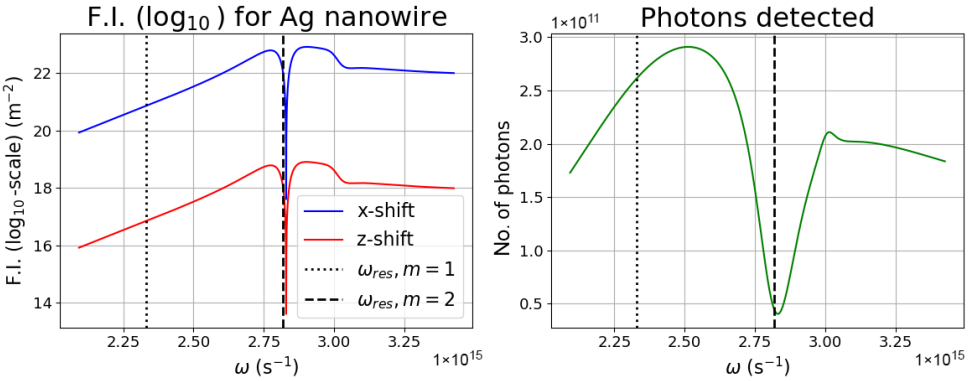

FIG. 9. Left: the Fisher information for the shift in the x direction and in the z direction, as a function of frequency ω of the incidence field, in $\log_{10}$ scale. Right: the total expected number of photons at the detector as a function of frequency ω. The incident power is 2.0 mW and for the dark-field illumination with the numerical apertures as stated in the text.

negligibile asymmetry. This causes a very small derivative $\partial_{\Delta x} I$, and hence much smaller Fisher information is obtained at $\omega = \mathrm{Re}(\omega_{\mathrm{res}}^{(2)})$. We are in a so-called *information dark state* [17].

VII. CAUSE OF THE INFORMATION DARK STATE

We investigate the cause of the information dark state by analyzing the scattering coefficients B_m [see Eq. (4.16)] as functions of ω. We will see that this dark state is caused by interference between the dipole and quadrupole modes.

The analysis is similar to the one done in Ref. [12]. We focus specifically on the behavior near the resonance frequency $\omega = \omega_{\mathrm{res}}^{(2)}$, which we abbreviate as ω_{res} from now on. For silver, the dominant scattering contributions come from modes with $m = \pm 1$ and $m = \pm 2$. The coefficients B_m with $|m| \geqslant 3$ are all at least an order of magnitude smaller. The coefficients $B_0(\omega)$, $B_1(\omega)$, and $B_2(\omega)$ are plotted in Fig. 12.

We also have the symmetry $B_m = B_{-m}$ for all m. From Fig. 12, it is clear that B_0 is small compared to B_1 and B_2. Moreover, coefficients with $m > 2$ (not shown in Fig. 12) are an order of magnitude smaller than B_1 and B_2.

At the resonance frequency ω_{res}, the imaginary part of B_2 changes sign from positive to negative, crossing zero at this frequency, i.e., $\mathrm{Im}(B_2(\omega_{\mathrm{res}})) = 0$. The reason this sign change occurs at the resonance frequency is because (as can be seen from Fig. 12) the coefficient B_2 is approximated by a Lorentzian curve close to ω_{res},

$$B_2(\omega) \approx \frac{-i\beta}{\omega - \omega_{\mathrm{res}}},$$

for some $\beta > 0$. The Lorentzian curve is more apparent for the $m = 2$ mode, since the imaginary part of the resonance frequency is an order of magnitude smaller than for $m = 1$. Hence, the sign change at $\omega = \omega_{\mathrm{res}}^{(2)}$.

To demonstrate how this sign change affects the symmetry of the scattering observed at the detector, we use a simplified model. In this model, the incident field consists of two plane waves illuminating the wire symmetrically from angles $-\theta$ and $+\theta$ relative to the z axis. The intensity of the interference of the plane waves has a maximum at $(+\Delta x, 0)^T$. This gives

$$H_y^{\mathrm{in}}(r, \varphi) = \sum_{m=-\infty}^{+\infty} A_m^{\mathrm{in}} J_m(k n_1 r) e^{im\varphi}, \tag{7.1}$$

with

$$A_m^{\mathrm{in}} = e^{-ikn_1 \Delta x \sin\theta} e^{im\theta} + e^{+ikn_1 \Delta x \sin\theta} e^{-im\theta} \tag{7.2}$$

$$= 2\cos(m\theta - kn_1 \Delta x \sin\theta). \tag{7.3}$$

Note that the A_m^{in} also depends on ω through the k. The scattering can be approximated by taking only the $m = \pm 1$ and $m = \pm 2$ terms from the expansion in Hankel modes.

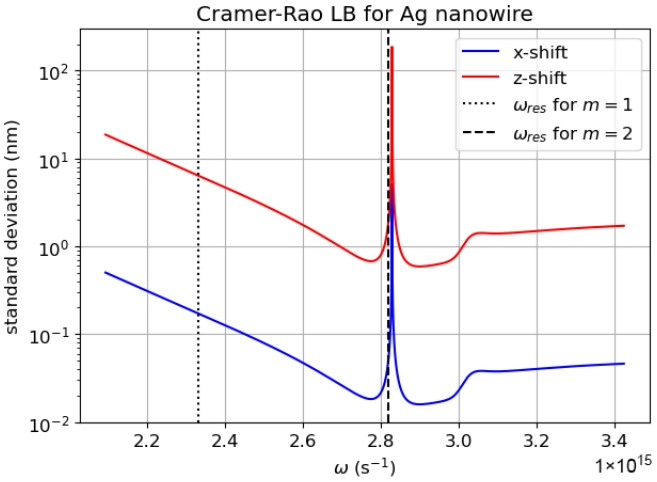

FIG. 10. The CRLB in units (nm) as a function of frequency ω. This is for the silver nanowire with $a = 20$ nm.

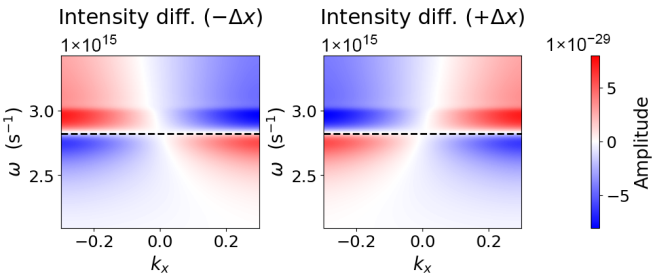

FIG. 11. Plot of the two quantities from Eq. (6.1), where the ω again is varied between 2.093×10^{15} and 3.425×10^{15} s^{-1} and k_x is between -0.3 and $+0.3$, corresponding to the NA of the detector. The black dashed line is at $\omega_{\mathrm{res}}^{(2)}$.

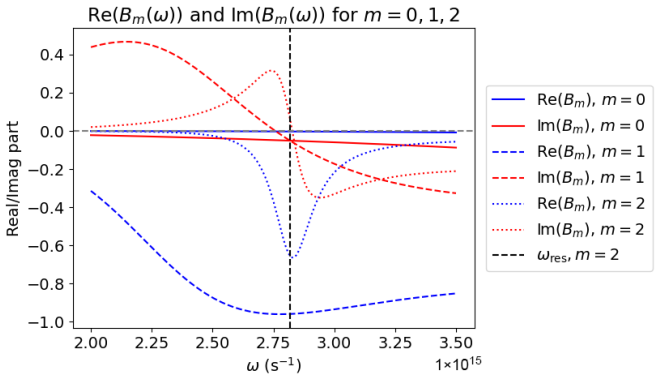

FIG. 12. Real and imaginary parts of the scattering coefficients B_m as functions of frequency ω, in the range from 2.0×10^{15} to 3.5×10^{15} s^{-1}. The resonance frequency $\omega_{\rm res}$ is indicated by the black dashed line.

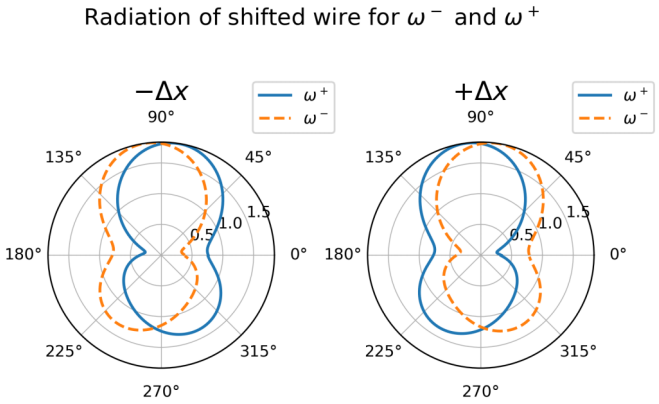

FIG. 13. Polar plot of the modulus of Eq. (7.7) as a function of φ in degrees, for two frequencies ω^- and ω^+. The plots are for a wire shifted by $-\Delta x$ (left) and a wire shifted by $+\Delta x$ (right).

We have

$$H_y^s(r,\varphi,\omega) \approx A_{-2}^{\rm in} B_{-2}(\omega) H_{-2}^{(1)}(kn_1 r) e^{-2i\varphi} + A_{-1}^{\rm in} B_{-1}(\omega) H_{-1}^{(1)}(kn_1 r) e^{-i\varphi} + A_1^{\rm in} B_1(\omega) H_1^{(1)}(kn_1 r) e^{i\varphi} + A_2^{\rm in} B_2(\omega) H_2^{(1)}(kn_1 r) e^{2i\varphi}. \quad (7.4)$$

Because we are interested in the far-field pattern, we use the following approximation for large z (see Eq. (21.27) in Ref. [18]),

$$H_m^{(1)}(z) \approx \sqrt{\frac{2}{\pi z}} e^{i(z - \frac{m\pi}{2} - \frac{\pi}{4})}, \quad (7.5)$$

which gives for r large,

$$H_m^{(1)}(kn_1 r) e^{im\varphi} \approx \sqrt{\frac{2}{\pi k n_1 r}} e^{ikn_1 r} e^{im(\varphi - \frac{\pi}{2})} e^{-i\frac{\pi}{4}}. \quad (7.6)$$

Then using the fact that $B_m = B_{-m}$ gives

$$H_y^s(r,\varphi,\omega) \approx \sqrt{\frac{2}{\pi k n_1 r}} e^{ikn_1 r} e^{-i\frac{\pi}{4}} \times \left[A_{-2}^{\rm in} B_2(\omega) e^{-2i(\varphi - \frac{\pi}{2})} + A_{-1}^{\rm in} B_1(\omega) e^{-i(\varphi - \frac{\pi}{2})} + A_1^{\rm in} B_1(\omega) e^{i(\varphi - \frac{\pi}{2})} + A_2^{\rm in} B_2(\omega) e^{2i(\varphi - \frac{\pi}{2})}\right]. \quad (7.7)$$

Let ω^- and ω^+ be the frequency where Im($B_2(\omega)$) is maximum and minimum, respectively. As is seen in Fig. 12, $\omega^- < \omega_{\rm res} < \omega^+$. We show in Fig. 13 the polar plot of the modulus of H_y^s as a function of φ for the case that $\Delta x =$ 100 nm and the angle of incidence for the two plane waves is $\theta = \pm 30^\circ$.

It can be seen from Fig. 13 that, although the spot is shifted in the same direction for both ω^- and ω^+, the radiation pattern almost flips its symmetry around the z axis. This is because the sign of the imaginary part of $B_2(\omega)$ changes between ω^- and ω^+, which causes a phase difference in the quadrupole ($m = \pm 2$) Hankel modes for ω^- and ω^+, and hence causes the flip in the far-field intensity pattern.

At the exact resonance $\omega = \omega_{\rm res}$ corresponding to $m = 2$, the Fisher information becomes zero. This can also be seen by looking at the scattering of the dipole and quadrupole modes. This is explained in detail in the Appendix. We have at the resonance that (see also the Appendix)

$$\frac{d}{d\Delta x} I(\varphi) \propto -4k_x \sin(2k_x \Delta x), \quad (7.8)$$

so at $\Delta x = 0$,

$$\left.\frac{d}{d\Delta x} I(\varphi)\right|_{\Delta x = 0} = 0. \quad (7.9)$$

We conclude that also in this approximative simplified model, we have an information dark state at exactly the resonance; i.e., the Fisher information for small lateral displacements vanishes. Furthermore, this holds for any angle of incidence of the plane waves and for all scattering angles, i.e., for all pixels.

As is shown in the Appendix, the fact that Eq. (7.9) holds for all pixels follows from the fact that $B_1(\omega_{\rm res}) B_2(\omega_{\rm res})^*$ is real. This is a special property that holds only for the case of the nanowire of Ag with radius 20 nm. For a nanowire with radius 20 nm made of potassium, for example, the plasmonic resonance is rather sharp (not as sharp as for Ag), but the phase of $B_1(\omega_{\rm res}) B_2(\omega_{\rm res})^*$ is approximately 5.25 rad and therefore the Fisher information does not vanish.

VIII. ASYMMETRIC ILLUMINATION

If the two incident plane waves have a phase difference of $\phi = \pi/2$, the amplitudes $A_1^{\rm in}$ en $A_2^{\rm in}$ become:

$$A_m = e^{-i\pi/4} e^{-ik_x \Delta x} e^{im\theta} + e^{i\pi/4} e^{ik_x \Delta x} e^{-im\theta}. \quad (8.1)$$

By following the computation in the Appendix with $\phi = \pi/2$, the term of the far-field intensity that depends on Δx becomes

$$I(\varphi) \propto 2\cos(2k_x \Delta x + \phi) = 2\cos(2k_x \Delta x + \pi/2) = -2\sin(2k_x \Delta x). \quad (8.2)$$

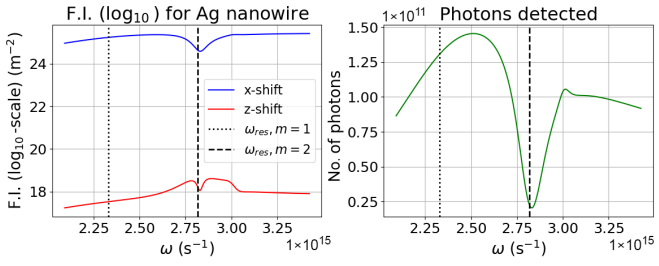

FIG. 14. Results for the silver nanowire illuminated by the spot obtained by illuminating with a pupil field with phase difference of $\pi/2$ between the left and right half of the pupil.

Hence, we now have

$$\frac{d}{d\Delta x} I(\varphi) \propto -4k_x \cos(2k_x \Delta x), \tag{8.3}$$

which gives nonzero Fisher information for $\Delta x = 0$, independently of the angle of incidence of the plane waves and for all scattering angles.

In fact, it can be shown that when the angle of incidence does not exceed 60°, for phase difference of $\pi/2$ between the two incident plane waves, the Fisher information is maximum (in all pixels) compared to any other phase difference between the incident plane waves.

This can be further confirmed by a numerical experiment. We illuminate the silver nanowire. Using the same dark-field illumination as before, we set the phase of the plane waves on the left side of the lens to $+\pi/2$. The phase of the plane waves on the right side stays 0. The Fisher information and expected number of photons are computed in the same way as for Fig. 9. The result for the asymmetric illumination is in Fig. 14, and the CRLB is plotted in Fig. 15.It can be seen in the figure that now there is no deep minimum in the Fisher information at the resonance frequency. The shallow minimum is due to a minimum in the number of photons at the detector at the resonance. The asymmetry "flip," as we had for the pupil field

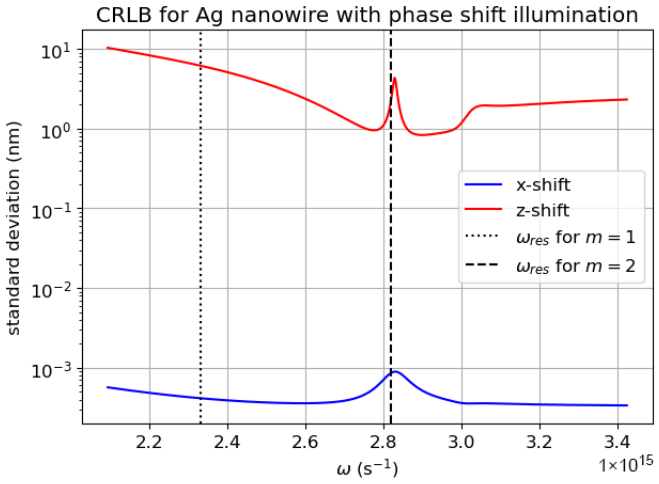

FIG. 15. The CRLB in units (nm) as a function of frequency ω, for the Ag nanowire and pupil field with phase shift $\pi/2$ between the left and right sides.

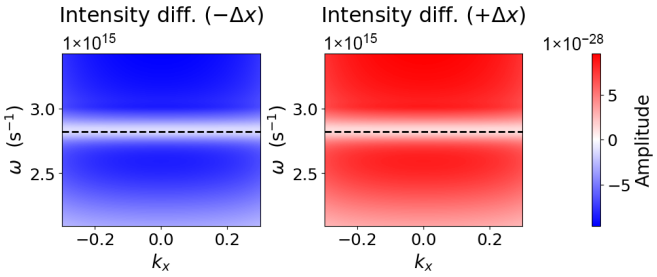

FIG. 16. Plot of the two quantities from Eq. (6.1) for the shifted silver nanowire, where ω again is varied between 2.093×10^{15} and 3.425×10^{15} s^{-1} and k_x is between -0.3 and $+0.3$. The black dashed line is at $\omega_{\text{res}}^{(2)}$. The result is for the difference of $\pi/2$ in the phase between the left and right half of the pupil field.

with uniform phase, does not occur in this case (see Fig. 16 and compare with Fig. 11).

IX. DISCUSSION

In the above analysis, a very specific set of parameters was chosen in order to induce a plasmonic resonance. As mentioned in Sec. V, the permittivities of the substrate (ε_1) and nanowire (ε_2) are chosen in such a way that we are close to the resonance condition for the electrostatic case (5.1). The radius of the nanowire is chosen to be small compared to the wavelength.

In this section, we briefly discuss how critical the parameter values are for the observed phenomena. For a substrate with index of refraction equal to $n_1 = 2.5$, an information dark state occurs, but at a different wavelength (see Fig. 17). In the figure, the resonance frequencies have been recomputed for this substrate index.

For these shorter wavelengths however, the Drude model for Ag is not as accurate as for longer wavelengths, as can be seen from Fig. 8. This is also why, in the previous analysis, the choice was made for a substrate with (very) high refractive index. Alternatively, the Lorentz-Drude model could be used to model the permittivity of Ag for smaller wavelengths as well [19].

In our analysis for the wire with radius $a = 20$ nm, taking the modes for $m = 1$ and $m = 2$ to approximate the scattered field was sufficiently accurate. However, when the radius of the wire becomes larger, more scattering terms need to

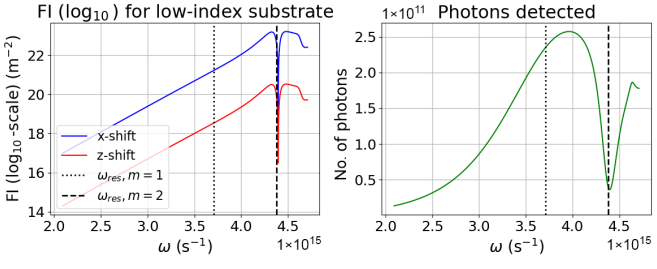

FIG. 17. Results for the silver nanowire inside a dielectric substrate with refractive index $n_1 = 2.5$. The quadrupole resonance now occurs for frequency $\omega = 4.380 \times 10^{15}$, corresponding to a wavelength of around $\lambda = 430$ nm.

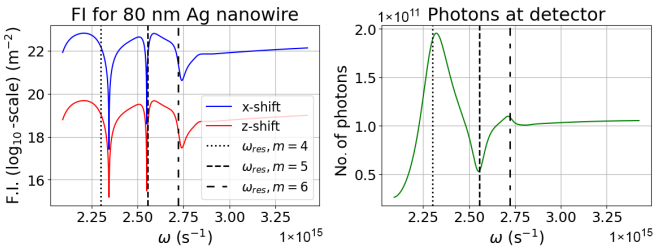

FIG. 18. Results for the silver nanowire with radius $a = 80\,\text{nm}$ inside a substrate with index $n_1 = 4.0$.

be added in the approximation. When we set the radius to $a = 80\,\text{nm}$, we see dark states around the resonance frequencies obtained for $m = 4$, $m = 5$, and $m = 6$ as well (The resonance frequencies for $m = 1$ up to $m = 3$ have a wavelength larger than 900 nm) (see Fig. 18).

Note that there is an offset between the $m = 4$ resonance frequency and the actual dark state: This is because this complex frequency has an imaginary part that is more than twice as large as the imaginary part for $m \geqslant 5$. The results for a nanowire with $a = 5\,\text{nm}$ are shown in Fig. 19. Note that the overall Fisher information is much lower than for the case $a = 20\,\text{nm}$. There is no dip in the number of detected photons at the $m = 2$ resonance frequency, but there is still an information dark state.

A plasmonic resonance of the nanowire can be used experimentally to determine extremely small lateral displacements Δx of the wire from the optical axis of the illuminating system, using dark-field illumination. By minimizing the difference between computed and measured pixel intensities, Δx can be retrieved with very low standard deviation. When the illumination is symmetric, the frequency should be chosen slightly off resonance to avoid the information dark state and utilize the local maximum of the Fisher information. It is seen in Fig. 10 that for laser power of 2 mW, the CRLB of Δx is below 0.1 nm for these frequencies. At the resonance frequency and very close to it, where the Fisher information has a sharp minimum, the CRLB is ∼3 nm for this laser power. A precision lower bound of ∼3 nm would already be too high in a typical semiconductor metrology setting.

When the illumination of the left and right half of the lens pupil differs by $\pi/2$, the dark state is eliminated and then the Fisher information is high and consequently the theoretical CRLB is as small as 0.001 nm for a range of frequencies at and close to the resonance (see Fig. 15).

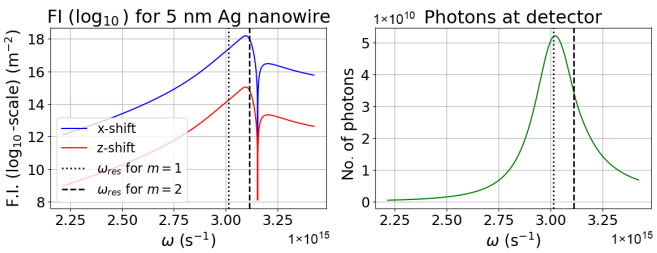

FIG. 19. Results for the silver nanowire with radius $a = 5\,\text{nm}$ inside a substrate with index $n_1 = 4.0$.

In retrieving Δx, one could minimize the difference between the simulated and measured amplitudes of the field in the pixels, or alternatively use the maximum likelihood estimator. Both methods are suitable in the case of Poisson noise, while the latter has the advantage that in the case of sufficiently many repeated measurements the CRLB for the standard deviation is achieved. Comparing different retrieval methods is a subject for further research.

X. CONCLUSIONS

In this paper, the effect of plasmonic resonances on the Fisher information with respect to small lateral and longitudinal displacements of a long silver nanowire was studied through a two-dimensional analytical model. First, the Fisher information and Cramér-Rao lower bound were explained for Poisson shot noise. The illumination and detection system was then explained, as well as the analytical model used to simulate sensitivitiy of the detected intensity to small displacements. A dark-field illumination system was used in order to separate the incidence field and the field scattered by the nanowire. The complex resonance frequencies of the plasmonic resonances occurring in a metallic nanowire were computed analytically.

Then, the Fisher information with respect to very small lateral and longitudinal displacements was computed as a function of frequency, for a nanowire of radius 20 nm made of Ag.

It was found that, although the Fisher information is enhanced for ω close to the real part of the magnetic quadrupole resonance frequency $\omega_{\text{res}}^{(2)}$, there is a sharp local minimum at the exact quadrupole resonance frequency. We have studied this by looking at the far-field scattering as a function of scattering angle for ω below, at, and higher than the quadrupole resonance frequency. From the radial dependence of the far field, it can be seen that the lateral translation of the nanowire induces an asymmetry. This asymmetry flips with respect to the z axis at the quadrupole frequency. At the exact quadrupole frequency, the flip occurs, and hence the scattered field shows little asymmetry for shifts in the two directions. Hence, at the resonance frequency we have an information dark state for lateral and longitudinal displacements.

Although the analysis was done for nanowire with a radius of 20 nm, the phenomenon occurs more generally and for different radii of the nanowire.

Finally, we have shown that the flip of the asymmetry can be prevented by changing the incident wave front. By introducing a phase shift of $\pi/2$ betwen the pupil fields in the left and right half of the pupil, the information dark state is eliminated. We have derived this first with a simplified analytical model, and confirmed this result with the full model.

In conclusion, plasmonic near resonances can be used to improve sensing for precise retrieval of far subwavelength displacements, when the frequency of the illumination is close to but not at the plasmonic resonance. However, exactly at resonance frequencies, the Fisher information is decreased by several orders of magnitude causing an unreliable estimation. By introducing a phase difference in the focused pupil field, this information dark state can be prevented and very accurate

displacement estimation can be obtained, even at the resonance frequency itself.

ACKNOWLEDGMENTS

The authors would like to thank Allard Mosk, Bram Verreussel, and Jacob Seifert for helpful discussions on Fisher information dark states. This research was supported by the Topconsortia voor Kennis en Innovatie (TKI) programme under Grant TKI-HTSM/22.0657.

DATA AVAILABILITY

The code used in the computations is available [20].

APPENDIX A: DERIVATION OF EQUATION FOR RESONANCE FREQUENCIES

We derive Eq. (5.2) by solving the Helmholtz equation for the infinite cylinder for TM polarization, with no incident field present. In this case, it means that we solve for the y component of $\mathbf{H}$ field. As before, the radius of the cylinder is given by a, and the refractive index of the cylinder by n_2. The refractive index of the surrounding medium is denoted by n_1. We have

$$\Delta H_y(\mathbf{r}) + k^2 n_1^2 H_y(\mathbf{r}) = 0, \quad r > a, \tag{A1}$$

$$\Delta H_y(\mathbf{r}) + k^2 n_2^2 H_y(\mathbf{r}) = 0, \quad r < a. \tag{A2}$$

On the boundary of the cylinder, we have the following matching conditions in cylindrical coordinates:

$$\lim_{r\uparrow a} H_y(r,\varphi) = \lim_{r\downarrow a} H_y(r,\varphi), \quad \lim_{r\uparrow a} E_\varphi(r,\varphi) = \lim_{r\downarrow a} E_\varphi(r,\varphi). \tag{A3}$$

We now want to rewrite the second condition in terms of H_y. Note that we have $E_\varphi = -\sin\varphi E_x + \cos\varphi E_z$. We use Faraday's law. For $\omega > 0$ the frequency and ε the permittivity (which is equal to $\varepsilon_1 = n_1^2$ inside the cylinder and $\varepsilon_2 = n_2^2$ outside the cylinder),

$$-i\omega\varepsilon(\mathbf{r})\mathbf{E} = \nabla \times \mathbf{H}. \tag{A4}$$

It follows that

$$E_x = \frac{1}{-i\omega\varepsilon(\mathbf{r})}\frac{\partial H_y}{\partial z}, \quad E_z = \frac{1}{i\omega\varepsilon(\mathbf{r})}\frac{\partial H_y}{\partial x}. \tag{A5}$$

If we rewrite the radial part of $\mathbf{E}$, we get

$$\begin{aligned} E_\varphi &= \frac{1}{i\omega\varepsilon(\mathbf{r})}\left\{\sin\varphi\frac{\partial H_y}{\partial z} + \cos\varphi\frac{\partial H_y}{\partial y}\right\} \\ &= \frac{1}{i\omega\varepsilon}\left\{\frac{\partial y}{\partial r}\frac{\partial H_y}{\partial z} + \frac{\partial x}{\partial r}\frac{\partial H_y}{\partial x}\right\} = \frac{1}{i\omega\varepsilon(\mathbf{r})}\frac{\partial H_y}{\partial r}. \end{aligned} \tag{A6}$$

Hence, the matching condition (A3) for the radial part of $\mathbf{E}$ becomes

$$\lim_{r\uparrow a}\frac{1}{\varepsilon_2}\frac{\partial H_y}{\partial r} = \lim_{r\downarrow a}\frac{1}{\varepsilon_1}\frac{\partial H_y}{\partial r}. \tag{A7}$$

We are looking for resonance solutions of Eqs. (A1) and (A2), so we have no incident field. We can thus write H_z as a Bessel wave inside the cylinder, and a Hankel wave outside the cylinder,

$$H_y(r,\varphi) = AH_m^{(1)}(kn_1 r)e^{im\varphi}, \quad r > a, \tag{A8}$$

$$H_y(r,\varphi) = BJ_m(kn_2 r)e^{im\varphi}, \quad r < a, \tag{A9}$$

where m is in $\mathbb{Z}$. The constants A and B are determined by plugging these fields into Eqs. (A3) and (A7). This gives a 2×2 system of equations

$$\begin{aligned} AH_m^{(1)}(kn_1 a) &= BJ_m(kn_2 a), \\ \frac{A}{\varepsilon_1}\frac{d}{dr}H_m^{(1)}(kn_1 a) &= \frac{B}{\varepsilon_2}\frac{d}{dr}J_m(kn_2 a). \end{aligned}$$

By using the fact that $\varepsilon_1 = n_1^2$ and that $\varepsilon_2 = n_2^2$ and taking the derivative with respect to r, we obtain

$$\begin{pmatrix} H_m^{(1)}(kn_1 a) & -J_m(kn_2 a) \\ \frac{k}{n_1}H_m^{(1)'}(kn_1 a) & -\frac{k}{n_2}J_m'(kn_2 a) \end{pmatrix}\begin{pmatrix} A \\ B \end{pmatrix} = \begin{pmatrix} 0 \\ 0 \end{pmatrix}.$$

A nonzero solution for A and B can only exist when this determinant equals zero. We obtain the equation

$$-\frac{k}{n_2}H_m^{(1)}(kn_1 a)J_m'(kn_2 a) + \frac{k}{n_1}J_m(kn_2 a)H_m^{(1)'}(kn_1 a) = 0. \tag{A10}$$

APPENDIX B: INTERFERENCE BETWEEN DIPOLE AND QUADRUPOLE MODES

At the exact resonance $\omega = \omega_{\text{res}}$, the Fisher information becomes zero. We explain this using the simplified model for the scattering as in Sec. VII. We also assume that the two incident plane waves can have a phase difference of ϕ, so

$$A_m^{\text{in}} = e^{-i\phi/2}e^{-ikn_1\Delta x\sin\theta}e^{im\theta} + e^{i\phi/2}e^{ikn_1\Delta x\sin\theta}e^{-im\theta}. \tag{B1}$$

We use

$$B_1(\omega_{\text{res}}) = -0.96 + 0.019i \approx -0.96, \tag{B2}$$

and for $B_2(\omega_{\text{res}})$ we approximate

$$B_2(\omega_{\text{res}}) \approx -0.66.$$

The terms with B_1 and B_2 in Eq. (7.7) are now grouped together. We write

$$\Phi = kn_1\Delta x\sin\theta + \phi/2. \tag{B3}$$

This gives the following expression for the scattered far field:

$$\begin{aligned} H_y^s(r,\varphi,\omega) \approx 2\sqrt{\frac{2}{\pi kn_1 r}}e^{ikn_1 r}e^{-i\frac{\pi}{4}} \\ \times \{B_1(\omega_{\text{res}})[e^{-i\Phi}\sin(\varphi-\theta) + e^{i\Phi}\sin(\varphi+\theta)] \\ - B_2(\omega_{\text{res}})\big[e^{-i\Phi}\cos(2(\varphi-\theta)) \\ + e^{i\Phi}\cos(2(\varphi+\theta))\big]\}. \end{aligned} \tag{B4}$$

The intensity of H_y^s as a function of φ is given by

$$\begin{aligned} I(\varphi) \propto |B_1(\omega_{\text{res}})|^2|e^{-i\Phi}\sin(\varphi-\theta) + e^{i\Phi}\sin(\varphi+\theta)|^2 \\ + |B_2(\omega_{\text{res}})|^2|e^{-i\Phi}\cos(2(\varphi-\theta)) \\ + e^{i\Phi}\cos(2(\varphi+\theta))|^2 \end{aligned}$$

$$+ 2\mathrm{Re}\{B_1(\omega_{\mathrm{res}})B_2(\omega_{\mathrm{res}})^* \times [e^{-i\Phi}\sin(\varphi-\theta) + e^{i\Phi}\sin(\varphi+\theta)] \times [e^{-i\Phi}\cos(2(\varphi-\theta)) + e^{i\Phi}\cos(2(\varphi+\theta))]\}. \quad \text{(B5)}$$

We have

$$\begin{aligned} I(\varphi) \propto\ & |B_1(\omega_{\mathrm{res}})|^2[\sin^2(\varphi-\theta) + \sin^2(\varphi+\theta) \\ & + 2\cos(2\Phi)\sin(\varphi-\theta)\sin(\varphi+\theta)] \\ & + |B_2(\omega_{\mathrm{res}})|^2[\cos^2(2(\varphi-\theta)) + \cos^2(2(\varphi+\theta)) \\ & + 2\cos(2\Phi)\cos(2(\varphi-\theta))\cos(2(\varphi+\theta))] \\ & + 2\mathrm{Re}\{B_1(\omega_{\mathrm{res}})B_2(\omega_{\mathrm{res}})^*[\sin(\varphi-\theta)\cos(2(\varphi-\theta)) \\ & + \sin(\varphi+\theta)\cos(2(\varphi+\theta)) \\ & + e^{-2i\Phi}\sin(\varphi-\theta)\cos(2(\varphi+\theta)) \\ & + e^{2i\Phi}\sin(\varphi+\theta)\cos(2(\varphi-\theta))]\}. \end{aligned} \quad \text{(B6)}$$

We now use that B_1 and B_2 are purely real. The approximation (B6) can be split in a part that is independent of Δx, and a part that depends on Δx. The part of the intensity that is dependent on Δx is given by

$$\begin{aligned} I(\varphi) \propto\ & 2\cos(2\Phi)\{|B_1(\omega_{\mathrm{res}})|^2\sin(\varphi-\theta)\sin(\varphi+\theta) \\ & + |B_2(\omega_{\mathrm{res}})|^2\cos(2(\varphi-\theta))\cos(2(\varphi+\theta)) \\ & + B_1(\omega_{\mathrm{res}})B_2(\omega_{\mathrm{res}})[\sin(\varphi-\theta)\cos(2(\varphi+\theta)) \\ & + \sin(\varphi+\theta)\cos(2(\varphi-\theta))]\}. \end{aligned} \quad \text{(B7)}$$

We can immediately see from Eq. (B7) that

$$\frac{d}{d\Delta x}I(\varphi) \propto -4k_x\sin(2\Phi). \quad \text{(B8)}$$

So when $\phi = 0$ and $\Delta x = 0$, we have $\Phi = 0$, and hence

$$\left.\frac{d}{d\Delta x}I(\varphi)\right|_{\Delta x=0} = 0. \quad \text{(B9)}$$

This gives Fisher information zero at the resonance for the simplified model. However, when there is a phase difference of $\phi = \pi/2$ between the incident plane waves, Eq. (B8) becomes

$$\frac{d}{d\Delta x}I(\varphi) \propto -4k_x\sin(2k_x\Delta x + \pi/2) = -4k_x\cos(2k_x\Delta x), \quad \text{(B10)}$$

and hence Eq. (8.3) holds for the derivative with respect to the displacement Δx.

[1] C. Mack, *Fundamental Principles of Optical Lithography: The Science of Microfabrication* (John Wiley & Sons, Chichester, West Sussex, 2007).

[2] N. Kumar, P. Petrik, G. K. Ramanandan, O. El Gawhary, S. Roy, S. F. Pereira, W. M. Coene, and H. P. Urbach, Reconstruction of sub-wavelength features and nano-positioning of gratings using coherent Fourier scatterometry, Opt. Express **22**, 24678 (2014).

[3] H. Deschout, F. C. Zanacchi, M. Mlodzianoski, A. Diaspro, J. Bewersdorf, S. T. Hess, and K. Braeckmans, Precisely and accurately localizing single emitters in fluorescence microscopy, Nat. Methods **11**, 253 (2014).

[4] Y. Shechtman, S. J. Sahl, A. S. Backer, and W. E. Moerner, Optimal point spread function design for 3D imaging, Phys. Rev. Lett. **113**, 133902 (2014).

[5] X. Wei, H. P. Urbach, and W. M. Coene, Cramér–Rao lower bound and maximum-likelihood estimation in ptychography with Poisson noise, Phys. Rev. A **102**, 043516 (2020).

[6] J. Seifert, Y. Shao, R. Van Dam, D. Bouchet, T. Van Leeuwen, and A. P. Mosk, Maximum-likelihood estimation in ptychography in the presence of Poisson–Gaussian noise statistics, Opt. Lett. **48**, 6027 (2023).

[7] Z. Xi, S. Konijnenberg, and H. P. Urbach, Information-efficient metagrating for transverse-position metrology, Phys. Rev. Appl. **14**, 014026 (2020).

[8] D. Bouchet, J. Seifert, and A. P. Mosk, Optimizing illumination for precise multi-parameter estimations in coherent diffractive imaging, Opt. Lett. **46**, 254 (2021).

[9] D. Bouchet, S. Rotter, and A. P. Mosk, Maximum information states for coherent scattering measurements, Nat. Phys. **17**, 564 (2021).

[10] M. Horodynski, D. Bouchet, M. Kühmayer, and S. Rotter, Invariance property of the Fisher information in scattering media, Phys. Rev. Lett. **127**, 233201 (2021).

[11] J. Hüpfl, F. Russo, L. M. Rachbauer, D. Bouchet, J. Lu, T. Kuhl, and S. Rotter, Continuity equation for the flow of Fisher information in wave scattering, Nat. Phys. **20**, 1294 (2024).

[12] Z. Xi and H. P. Urbach, Magnetic dipole scattering from metallic nanowire for ultrasensitive deflection sensing, Phys. Rev. Lett. **119**, 053902 (2017).

[13] Z. Xi and H. P. Urbach, Retrieving the size of deep-subwavelength objects via tunable optical spin-orbit coupling, Phys. Rev. Lett. **120**, 253901 (2018).

[14] J. J. Bowman, T. B. Senior, and P. L. Uslenghi, *Electromagnetic and Acoustic Scattering by Simple Shapes* (Hemisphere Publishing Corporation, New York, 1987), revised ed.

[15] L. Novotny and B. Hecht, *Principles of Nano-Optics* (Cambridge University Press, Cambridge, 2012), 2nd ed.

[16] See Supplemental Material at http://link.aps.org/supplemental/10.1103/m4cm-545j for animations of the fields as functions of time, and also as functions of the frequency.

[17] A. P. Mosk (personal communication).

[18] A. Zangwill, *Modern Electrodynamics* (Cambridge University Press, Cambridge, 2013).

[19] A. D. Rakić, A. B. Djurišić, J. M. Elazar, and M. L. Majewski, Optical properties of metallic films for vertical-cavity optoelectronic devices, Appl. Opt. **37**, 5271 (1998).

[20] J. B. P. de Graaff, *plasmonic-nanowire* (GitLab repository). Delft University of Technology (TU Delft), 2025. Available at https://gitlab.tudelft.nl/J.B.P.deGraaff/plasmonic-nanowire. Accessed 12 Nov 2025.